Transient melting at the nanoscale: a continuum heat transfer and non-equilibrium molecular dynamics approach

Francesc Font*,† and Fernando Bresme*,‡

†*Department of Physics, Universitat Politècnica de Catalunya, Av. Dr. Marañon 44-50, 08028 Barcelona, Spain*

‡*Department of Chemistry, Imperial College London, SW7 2AZ, London, UK*

E-mail: francesc.font@upc.edu; f.bresme@imperial.ac.uk

Abstract

Transient melting is an ubiquitous phenomenon in nature, which plays an increasingly important role in the processing of nanomaterials. A sound theoretical description of this process is therefore important, both from fundamental and applied points of view. We present a numerical study of transient melting in simple atomic solids using both, continuum theory based on the heat diffusion equation and transient non-equilibrium molecular dynamics simulations. We show that continuum theory provides an accurate description of relevant properties, temperature relaxation, time dependent internal energy and dynamics of the melting front. However, deviations between the continuum approach and the molecular dynamics simulations are observed in ps timescales depending on the initial temperature used to melt the solid. These deviations are due to the emergence of new timescales associated to the activated character of the melting process. Consistently with this notion, we observe that the closer the initial temperature to the melting temperature of the solid, the longer the time it takes for the system

to converge to the continuum solution. For systems investigated here we find a delay in the recovery of the continuum solution of $\lessapprox 5$ to $\lessapprox 80$ ps for initial temperatures between 40% to 25% above the melting temperature of the solid, respectively. We find that the combination of continuum theory and molecular dynamics simulations provides a useful approach to quantify the temperature relaxation and the melting temperature of materials using short molecular dynamics trajectories.

1 Introduction

The heat diffusion equation (HDE) provides a powerful approach to study heat transfer at stationary and transient conditions. There are a number of macroscale problems of relevance in engineering that can be solved using analytical methods by mapping the system of interest to suitable geometries.[1] When this is not possible, numerical methods can be employed and implemented in finite element codes that enable the investigation of fairly complex structures. The development of nanodevices is driving ongoing efforts to describe heat transfer at the nanoscale, particularly to account for the mechanisms of heat transport of nano/micro systems. Current problems in the description of nanoscale heat transport were highlighted recently.[2] Interfaces become important at small nanometer length scales, and the use of continuum models typically requires knowledge of interfacial properties, which are not easily accessible.[3,4] Hence, the combination of continuum and molecular approaches reveals itself as a powerful and promising approach to develop numerical methods to study nanoscale heat transfer. One way to combine both approaches consists in coupling the continuum and atomistic descriptions into a single multiscale simulation method. Typically, these methods use molecular dynamics in localized regions of the computational domain where interface effects, *e.g.* grain boundaries or material defects, may play a role, while continuum-based governing equations are used in regions of the domain where the continuum assumption holds (see ref.[5] and references therein). Our focus in this work, is the analysis of continuum methods to describe thermal transport in melting processes at atomistic scales. Our conclusions should

be relevant to current efforts devoted to coupling simulation techniques.

The description of transient processes in nanoscale systems is a subject of current interest.[2,6] The heating of nanocrystals with high power lasers and the subsequent transient melting has been studied experimentally.[7] Computer simulations of related systems have also been reported.[8,9] The HDE offers a route to model the physical behavior of transient melting, and this approach has been extended to take into account the depression of the melting temperature with particle radius, by considering the Gibbs-Thomson equation.[10–12] These works reported interesting results regarding the variation of the melting behavior as the particle size decreases and fully melts, pointing towards an acceleration of the melting. Also, a prediction of the melting times and their scaling with the particle radius was reported using the HDE solution. Expanding these analyses to investigate the late stages of the melting process may require the use of non-continuum theories to incorporate *e.g.* interfacial conductance effects and changes in the thermal conductivity of the coexisting phases [13]. Molecular simulations provide a complementary approach to investigate this problem, and to assess the accuracy of the approximations adopted to solve the HDE at molecular scales.[3,14] Further, simulations can be used to gain insight into the molecular structure of the melting fronts that determine the heat transport across the interfaces,[15] as well as to calculate pseudo-experimental data, which can be implemented in the HDE approach, hence expanding its capabilities. The usefulness of the molecular simulations has been demonstrated in the investigation of the short time transient cooling of crystals.[16] Deviations between the continuum calculations and the simulations were found at very short times, *i.e.* at conditions that deviated significantly from equilibrium.

In this work we present an investigation of the transient melting of atomic crystals using both the HDE and transient non-equilibrium molecular dynamics simulations. We assess the accuracy of the HDE implementation to describe the simulation data, and solve the HDE using appropriate boundary conditions that take into account finite size effects. The article is structured as follows: firstly, we describe our simulation approach and the theoretical

model, which is based on the classical heat transfer theory. The later is extended to take into account melting in finite domains, which are relevant in small systems and the molecular simulation set up. A discussion of our main results follows. We close the paper with our main conclusions.

2 Transient non-equilibrium molecular dynamics simulations

We performed transient non-equilibrium simulations in order to test the accuracy of the continuum approach given by the heat diffusion equation. The simulations were performed with the truncated and shifted Lennard-Jones (LJ) potential,

$$U(r) = \begin{cases} 4\epsilon \left[\left(\frac{\sigma}{r}\right)^{12} - \left(\frac{\sigma}{r}\right)^{6} \right] - U(r_c) & \text{for } r \leq r_c \\ 0 & \text{for } r > r_c \end{cases} \tag{1}$$

where σ is the particle diameter, ϵ the interaction strength and r_c the potential cut-off. The LJ model has been characterized extensively. In particular, the melting line was computed in previous studies.[17] Moreover, the parameters of the LJ model has been fitted to describe thermodynamic and elastic properties of face centered cubic metals, such as gold. It was found that its accuracy is similar to that of tight-binding and embedded atom models, at a fraction of the computational cost.[18] The transferability and generality of this model to describe a wide range of solids makes it a good starting point for our investigation. The simulations reported here were conducted with a cut-off for the pair interactions of $r_c = 6\sigma$. Short cut-offs give rise to a non-monotonic dependence of the melting temperature, and therefore they were avoided. For 6σ the melting temperature of the solid agrees closely with that obtained with the full potential.[17]

All the properties reported hereafter are given in reduced units, namely we use σ and

ϵ as units of length and energy, respectively. We set the reduced timestep to 0.002, which corresponds to $\sim$0.004 ps using $\epsilon = 1.65 \times 10^{-21}$ J and $\sigma = 3.41$ Å values, characteristic of argon.[19] The equations of motion were integrated using the velocity Verlet algorithm and the parallel code LAMMPS.[20] All the simulations were performed using periodic boundary conditions in all directions.

To model the transient melting process we generated an FCC lattice with the {0,0,1} plane perpendicular to the z axis of the simulation box. We investigated different system sizes consisting of 14 unit cells in the x and y direction, and a variable number of cells, $14 - 112$, in the direction of the heat flux, z. In total, we studied 4 systems, $(N_x, N_y, N_z) = (14, 14, 14), (14, 14, 28), (14, 14, 56), (14, 14, 112)$, which involve different number of particles, 10976, 21952, 43904 and 87808. The initial configuration was equilibrated for $\sim 10^5$ timesteps in the NPT ensemble at temperatures below the melting one, $T^* = 0.8$ for $T_m^* = 1$. The simulations were performed at the coexistence pressure, $P^* = 3.893$ for $T_m^* = 1$. The coexistence pressures and densities for this temperature were calculated using equations (19)-(21) in reference.[17] A thermostatting region with a thickness of 1.5σ, was set up in the geometric center of the simulation box. The particles entering this region during the simulation, were thermostatted every time step using a simple velocity rescaling approach. Following each rescaling event we reset the total momentum of the simulation box. Using this procedure a transient heat flux was induced along the crystal. The crystal melts gradually, from the region where the thermostat is applied, outwards. At the end of the transient process the whole system becomes a liquid with an average temperature equal to the temperature set initially in the thermostat. The temperature of the thermostat was set to $T^* = 1.4$, hence higher than the melting temperature $T_m^* = 1$. We also performed additional simulations setting the thermostat at $T^* = 1.25$, in order to asses the impact of the temperature of the thermostat on the melting process.

The temperature profile was computed using the equipartition principle,

$$\frac{1}{k_B T(l)} = \left\langle \frac{3N}{\sum_{i=1}^{N\in l} \frac{\mathbf{p}_i^2}{m_i}} \right\rangle \tag{2}$$

partitioning the system in 500 layers. The local temperature in layer l was computed by performing the sum in equation (2) over the particles inside that layer. $\mathbf{p}_i$ and m_i in equation (2) represent the momentum and the mass of particle i, respectively.

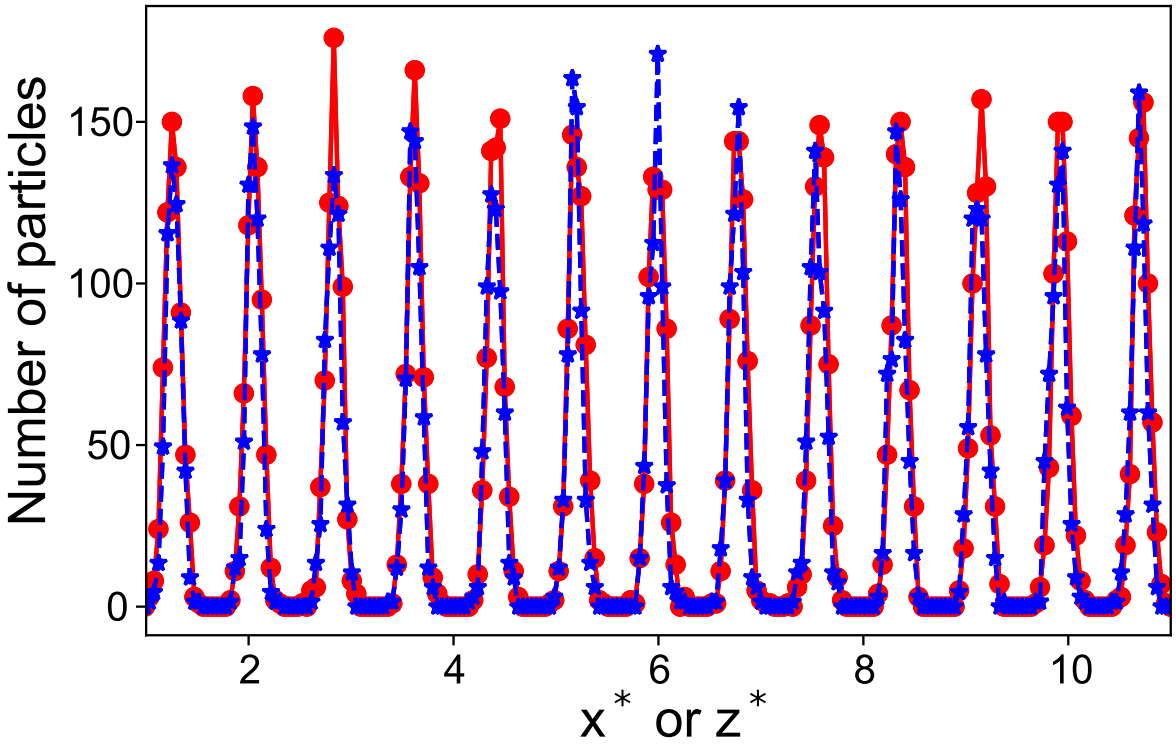


Figure 1: Histogram of the number of particles in the x (red symbols) and z (blue symbols) directions, for the system represented in Figure 2. The number of particles for the z component has been multiplied by a factor of 1.5 and it has been shifted in the z direction by 0.44σ units to facilitate the comparison between the two histograms.

We performed initial tests of the simulation of transient melting at constant volume. At constant volume the increase in the temperature of the system driven by the application of the thermostat results in a concomitant increase of the pressure and the melting temperature of the solid. Hence, we implemented a barostat (Berendsen barostat[21]) to ensure the transient

process proceeded at constant pressure, and the box volume could change as a result of the thermal expansion process. The box length in the direction of the heat flux, z, was allowed to change independently from the other two directions, x, y. The time constant for the stress damping parameter was set to 2, in LJ units. The formation of the crystal-liquid interface results in an interfacial tension that acts as a negative pressure in the direction tangential to the interface. For large systems, the impact of this pressure is expected to be small. This effect can be assessed by calculating the pressure difference between normal and tangential components of the pressure, due to the presence of the liquid-crystal interface,

$$\Delta P = P_{zz} - \left(\frac{P_{xx} + P_{yy}}{2} \right) = \frac{2\gamma}{L_z} \tag{3}$$

where $P_{\alpha\alpha}$ are the diagonal components of the pressure tensor, L_z is the length of the box along the direction of the heat flux and γ is the liquid-solid interfacial tension. The interfacial tension of the truncated version of the Lennard-Jones potential for a range of temperatures, $T^* = 0.6 - 1.5$, relevant to us, varies from $\gamma^* = 0.5$ to 0.85[22] for the $\{001\}$ face studied here. Hence, ΔP^* is expected to change from 0.0062-0.077, which is a small change as compared with the average pressure of the system, $P^* = 3.893$. We ensured that the implementation of the pressure scheme reproduced an isotropic crystal structure. Figure 1 shows the histogram of the number of particles along the x and z axes, parallel and perpendicular to the interface plane, respectively, and for a representative configuration containing a solid-liquid interface (see bottom panel in Figure 2). We selected for our analysis particles in a section of the solid phase (left hand side of the bottom panel in Figure 2). The analysis of the histograms (see Figure 1) shows that the atom positions along parallel, x, and perpendicular, y, directions agree with each other, indicating that the use of the barostat does not introduce an anisotropy in the solid. Hence, in subsequent simulations we used the NPT scheme discussed above.

The thermal conductivities of the coexisting phases, liquid and solid, were computed

using the Green-Kubo equation:[23]

$$k = \frac{V}{3k_B T^2} \int_0^{t_m^*} dt \, \langle \mathbf{J}_q(t) \cdot \mathbf{J}_q(0) \rangle \,, \tag{4}$$

where, V is the volume of the simulation cell, T the temperature and $\mathbf{J_q}$ is the microscopic energy flux, which is defined by,[24]

$$\mathbf{J}_q = \frac{1}{V} \left[\sum_i \mathbf{v}_i e_i + \frac{1}{2} \sum_{i \neq j} \left(\mathbf{f}_{ij} \cdot \mathbf{v}_i \right) \mathbf{r}_{ij} \right], \tag{5}$$

where e_i represents the sum of the kinetic and potential energies of atom i, $\mathbf{v}_i$ is the velocity of atom i and $\mathbf{f}_{ij}$ the force between atoms i and j. All the thermal conductivity computations were performed at equilibrium conditions in the microcanonical ensemble (NVE). The upper limit for the integration of the correlation function (see equation 4) was set to $t^*_{max} = 2.75$. The integral of the autocorrelation function reaches a plateau for times shorted than this (see Figure 3). In addition, we calculated the heat capacity at constant volume and the enthalpy of melting, which were used as input in the calculations performed with the HDE. The heat capacity was obtained by performing a series of simulations at different temperatures in the canonical ensemble (NVT). The heat capacity was extracted from the numerical derivative of the internal energy with respect to the temperature.

3 Melting model from classical heat transfer theory

Classical heat transfer theory, based on the continuum approach, provides a well-known description of phase change processes. The mathematical formulation of the problem involves heat equations for the solid and liquid phases and a condition at the solid-liquid interface, the Stefan condition, which describes the position of the phase change front. At the moving phase change boundary, $z = s(t)$, the temperature is fixed at the constant bulk phase change temperature, T_m.

Melting of a semi-infinite slab (IS). We consider first the melting of a one-dimensional semi-infinite slab occupying $z \geq 0$, where the phase change is driven by a constant temperature, T_h, imposed at the boundary $z = 0$. The slab, initially at a uniform temperature below the melting point, $T_0 < T_m$, will suddenly start melting from $z = 0$.

The governing equations for the temperature in the liquid and the solid region are

$$c_l \rho_l \frac{\partial T_l}{\partial t} = k_l \frac{\partial^2 T_l}{\partial z^2} \quad \text{on} \quad 0 < z < s(t) \ , \tag{6}$$

$$c_s \rho_s \frac{\partial T_s}{\partial t} = k_s \frac{\partial^2 T_s}{\partial z^2} \quad \text{on} \quad s(t) < z < \infty \ . \tag{7}$$

where the subscripts 'l' and 's' indicate liquid and solid, respectively, $s(t)$ is the position of the melting front, T the temperature, ρ the density, k the thermal conductivity and c the heat capacity. Considering the energy balance at the solid-liquid interface gives,

$$\rho_s L_m \frac{ds}{dt} = k_s \left. \frac{\partial T_s}{\partial z} \right|_{z=s(t)} - k_l \left. \frac{\partial T_l}{\partial z} \right|_{z=s(t)} \ . \tag{8}$$

where L_m is the enthalpy of fusion. The appropriate boundary and initial conditions for equations (6)-(7) are $T_l(0,t) = T_h$, $T_l(s(t),t) = T_s(s(t),t) = T_m$, $T_s(z,0) = T_0$ and the initial condition for (8) is $s(0) = 0$, where T_m and T_0 are the melting temperature and the temperature of the hot source applied to the solid phase. Note that the model formulation (6)-(7) assumes $\rho_l = \rho_s$. Typically, the density difference between the solid and the liquid phase is small and its effect on the heat transport and melt front evolution is usually neglected. Inclusion of density change would result in an advection term in (7), which accounts for heat transport due to the displacement of the liquid upon expansion, and a kinetic energy term proportional to $(ds/dt)^3$ in (8) (see ref.[25]). In some specific cases, such as in spherical nanoparticles, the depression of the melting temperature can have a magnifying effect on these terms, and the density change needs to be accounted for in the formulation of the model.[11] In our continuum model we ignore the thermal conductance (Kapitza resistance) contributions of the solid-liquid interface. This approach is accurate for the systems inves-

tigated here, where the thermal resistance results in a negligible temperature "jump" (see Results section, Figure 8). This result is consistent with previous simulations reported in [26] where the thermal conductance ~~of a Lennard Jones crystal at T^* = 0.67 was found to be > 400 MW/m^{2}K, leading to temperature differences of the order of ΔT^* = 0.007 for heat fluxes similar to those employed here~~.

The model defined by equations (6)-(8) with the specified boundary conditions has an exact analytical solution, which is usually referred to as the Neumann solution. [27] The temperatures in the liquid and the solid take the form,

$$T_l(z,t) = T_h - (T_h - T_m)\,\frac{\mathrm{erf}\,\left(z/2\sqrt{\alpha_l t}\right)}{\mathrm{erf}\,(\lambda)}\,, \tag{9}$$

$$T_s(z,t) = T_0 + (T_m - T_0)\,\frac{\mathrm{erfc}\,\left(z/2\sqrt{\alpha_s t}\right)}{\mathrm{erfc}\,\left(\lambda\sqrt{\alpha_l/\alpha_s}\right)}\,, \tag{10}$$

and the position of the melting front is given by,

$$s(t) = 2\lambda\sqrt{\alpha_l t}\,, \tag{11}$$

where $\alpha_l = k_l/c_l\rho_l$ represents the thermal diffusivity of the liquid. The constant λ is the solution of the transcendental equation,

$$\frac{1}{\beta_l \exp\left(\lambda^2\right)\mathrm{erf}\,(\lambda)} - \frac{1}{\beta_s \exp\left(\lambda^2\alpha_l/\alpha_s\right)\mathrm{erfc}\,\left(\lambda\sqrt{\alpha_l/\alpha_s}\right)} = \lambda\sqrt{\pi}\,, \tag{12}$$

where $\beta_l = L_m/c_l(T_h - T_m)$ and $\beta_s = L_m/c_s(T_m - T_0)$ are the Stefan numbers of the liquid and the solid phase, respectively, and α_s the thermal diffusivity of the solid.

The total energy change in the system is given by the sum of the energy change due to the temperature change in the solid and in the liquid (e_s and e_l, respectively), and the energy corresponding to the latent heat of the liquid phase (e_{lat}). Taking T_0 (temperature

of the slab at $t = 0$) as a reference temperature corresponding to a reference internal energy set to zero, the time evolution of the energy change in the liquid and the solid phase due to the temperature change is obtained from,

$$e_l(t) = \int_0^{s(t)} \rho_s c_s \left(T_m - T_0\right) dz + \int_0^{s(t)} \rho_l c_l \left(T_l(z,t) - T_m\right) dz \,, \tag{13}$$

$$e_s(t) = \int_{s(t)}^{\infty} \rho_s c_s \left(T_s(z,t) - T_0\right) dz \,. \tag{14}$$

Inserting equations (9)-(10) in (13)-(14) gives,

$$e_l = \frac{\rho_s L_m s(t)}{\beta_s} + \frac{\rho_s L_m s(t)(1 - e^{-\lambda^2})}{\beta_l \sqrt{\pi} \lambda \mathrm{erf}\lambda} \,, \tag{15}$$

$$e_s = \frac{\rho_l L_m s(t)}{\beta_s \sqrt{\pi} \sqrt{\alpha_l/\alpha_s} \lambda e^{\alpha_l t^2/\alpha_s} \mathrm{erfc}\lambda} \,. \tag{16}$$

The energy corresponding to the latent heat is $e_{\mathrm{lat}} = \rho_l \, L_m \, s(t)$.[25] Note that we are using a semi-infinite domain and we only take into account half of the space. In order to compare with the results from the MD simulation we will have to multiply the energy by 2. In addition, we multiply the energy by the cross-sectional area of the MD cell. Thus, the total energy in the system is given by,

$$\Delta E(t) = 2 \, A \left(e_l + e_s + e_{\mathrm{lat}}\right). \tag{17}$$

Melting of a finite slab (FS). The formulation of the model in a semi-infinite domain allows us to obtain an exact solution for the temperature of the solid and the liquid and the position of the melting front. However, the fact that the model is defined in a semi-infinite domain means that the comparison with the simulation results, where the simulation cell has a finite size, might not be straightforward. To address this point we introduce a modified model to take into account finite size effects. Firstly, we re-define the domain of

Eq. (7) for $[s(t), L]$ where $L = L_z/2$ (with L_z being the length of the MD cell along the z-axis). Secondly, we replace the far field boundary condition $T_s|_{z\to\infty} \to T_0$ by a zero flux boundary condition, namely,

$$\left.\frac{\partial T_s}{\partial z}\right|_{z=L} = 0 \ . \tag{18}$$

Physically, this boundary condition represents an insulated boundary, which is consistent with the periodic boundary conditions used in the MD simulation. The introduction of the new boundary conditions, $T_l(0,t) = T_h$, $T_l(s(t),t) = T_s(s(t),t) = T_m$ and (18), means that the solution of equations (6)-(8) describing the melting of a finite slab of length L, can not be performed analytically, instead the equations must be solved numerically.

The numerical solution of partial differential equations defined in moving domains can be troublesome. One way to simplify the numerical implementation is by introducing new coordinate variables that transform the moving domain into a fixed domain.[28] As a result, the domain does not have to be updated every time step, while the equation becomes more complicated. We introduced the variables $\xi = z/s$ and $\eta = (z-s)/(L-s)$, which transform the domains $[0, s(t)]$ and $[s(t), 1]$ into the unit domain $[0, 1]$. The resulting equations were solved using second-order central differences and a semi-implicit backward Euler scheme, solving implicitly for T_s and T_l, and explicitly for $s(t)$.[29] Since the liquid phase has initially zero thickness its temperature is undefined at $t = 0$. To overcome this problem we conducted a small time asymptotic analysis, following reference,[30] to obtain an expression for T_l at some small time $t > 0$ to initialize our numerical scheme. The numerical scheme was implemented in Matlab.[31] Finally, in order to find $\Delta E(t)$ we introduced T_s, T_l and $s(t)$ from the numerical solution in equations (13)-(14) and evaluated the corresponding integrals numerically using the Matlab function `trapz`.

4 Results

We show in Figure 2 a sequence of snapshots obtained using the transient NPT method. The snapshots capture different stages of the transient melting process. The simulations were performed at constant pressure $P^* = 3.893$, starting from pre-equilibrated systems at $T^* = 0.8$ and subsequently, setting the thermostat in the middle of the simulation cell to $T^* = 1.4$. During the transient process the melting front advances along the z direction, and the volume of the simulation cell changes to accommodate the thermal expansion induced by the increasing average temperature of the system. For the sequence represented in Figure 2 the average temperature changes from 0.8 to 0.94, and the simulation cell changes from $L_z^* =$ 175.63 to 182.49.

Previous studies found that continuum theories based on the Fourier law (or extensions of this law leading to hyperbolic forms of the heat conduction equation) fail at very short times and small length scales. Typically at times shorter than the heat flux relaxation time, τ_{J_q}, and lengths smaller than the phonon mean-free path.[16,32–34] To gain insight into the relevant time scales for our system we estimated the heat relaxation time from the analysis of the heat flux autocorrelation function, which was calculated using equilibrium molecular dynamics simulations of the solid and liquid phases,

$$\tau_{J_q} = \int_0^{t_m} \frac{\langle \mathbf{J}_q(t) \cdot \mathbf{J}_q(0) \rangle}{\langle \mathbf{J}_q(0) \cdot \mathbf{J}_q(0) \rangle} \, dt \,, \tag{19}$$

where the brackets indicate a time correlation function, and $\mathbf{J}_q(t)$ and $\mathbf{J}_q(0)$ represent the heat flux at two different times, while t is the correlation time. The Green-Kubo equations were used in bulk systems at coexistence conditions. The computations of liquid and solid phases were performed separately. We show in Figure 3 the normalized correlation functions (integrand of equation (19)) for the solid and liquid phases at coexistence conditions corresponding to $T^* = 1$. The heat flux features an exponential decay that is slower for the solid phase. The relaxation time was estimated from the integral given in equation (19).

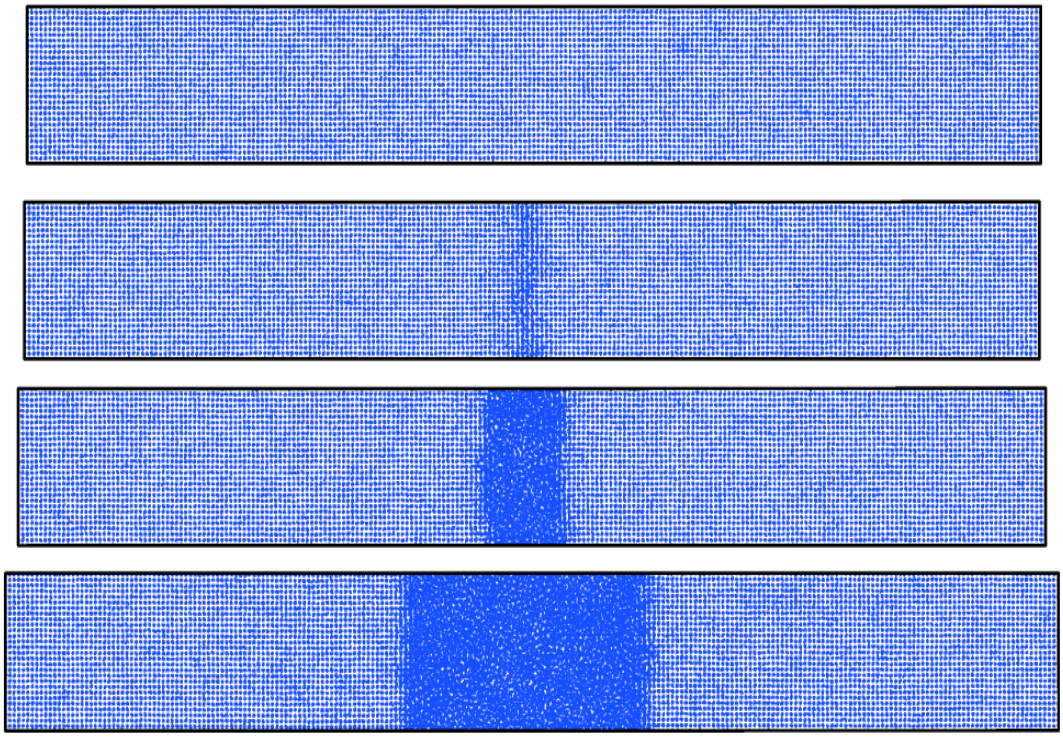


Figure 2: Snapshots of the initial configuration of a LJ solid consisting of 87808 atoms. The initial temperature and pressure were $T^* = 0.8$ and $P^* = 3.893$. The thermostat temperature in the middle of the simulation cell corresponds to $T^* = 1.4$. The melting temperature of the solid at this pressure is $T^* = 1.0$.[17] The snapshots show a sequence of configurations during the transient process at different times: $t^* = 0, 2, 20, 200$.

We collect our results in Table 1. The relaxation time is fast, being in all cases in the sub-picosecond timescale. As noted before deviations between the solution obtained with the continuum approach and with MD are expected at times shorter than τ_{J_q}. Advancing the discussion below, we did also find deviations between the simulation and continuum results at longer time scales. The physical origin of these deviations is discussed below.

We show in Figure 4 the time dependence of the transient melting process. The panels in Figure 4 illustrate the variation of temperature and density with time. The temperature diffuses from the center of the simulation cell outwards, and the solid melts during this process. The time evolution of the melting front can be extracted from the analysis of the

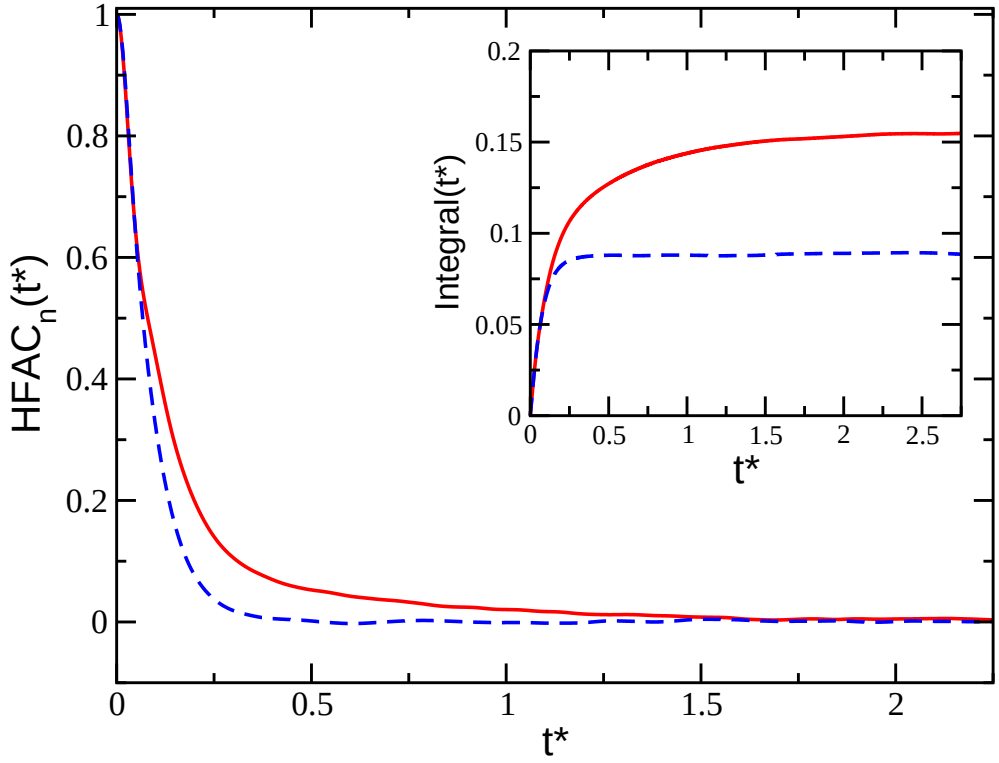


Figure 3: Normalized heat flux autocorrelation functions $\mathrm{HFAF}_n(t^*) = \langle \mathbf{J}_q(t^*) \cdot \mathbf{J}_q(0) \rangle \,/\, \langle \mathbf{J}_q(0) \cdot \mathbf{J}_q(0) \rangle$ for solid (solid line) and liquid phases (dashed) at coexistence conditions, $T^* = 1.0$. The inset shows the integral of the correlation function (see eqn. (19)).

temperature profiles, by identifying the position at which the temperature of the profile is equal to the melting temperature. Our simulation results for the position of the front with time, $s(t)$, are collected in Figure 5, along with the theoretical predictions using the analytical solution of the semi-infinite slab (IS) model and the numerical solution for the finite slab (FS) model.

The simulation results for long simulation boxes can be described accurately using the solution of the IS model (see Eq. (11)) in the interval $10 < t^* < 500$ and $1 < t^* < 1000$ for the 56 (panel (c)) and the 112 (panel (d)) system sizes, respectively. These results validate

Table 1: Properties of the systems simulated in this work. T_m^*, P^*, ρ^*, c^*, λ^* and $\tau_{J_q}^*$ represent the melting temperature, coexistence pressure, coexistence density, heat capacity at constant pressure, thermal conductivity and heat flux relaxation time, respectively.

T_m^*	Phase	P*	ρ^*	c^*	λ^*	$\tau_{J_q}^*$
1.0	Liquid	3.893	0.9186	4.4402	9.34 ± 0.21	0.09
1.0	Solid	3.893	1.0062	4.1604	12.33 ± 0.32	0.16

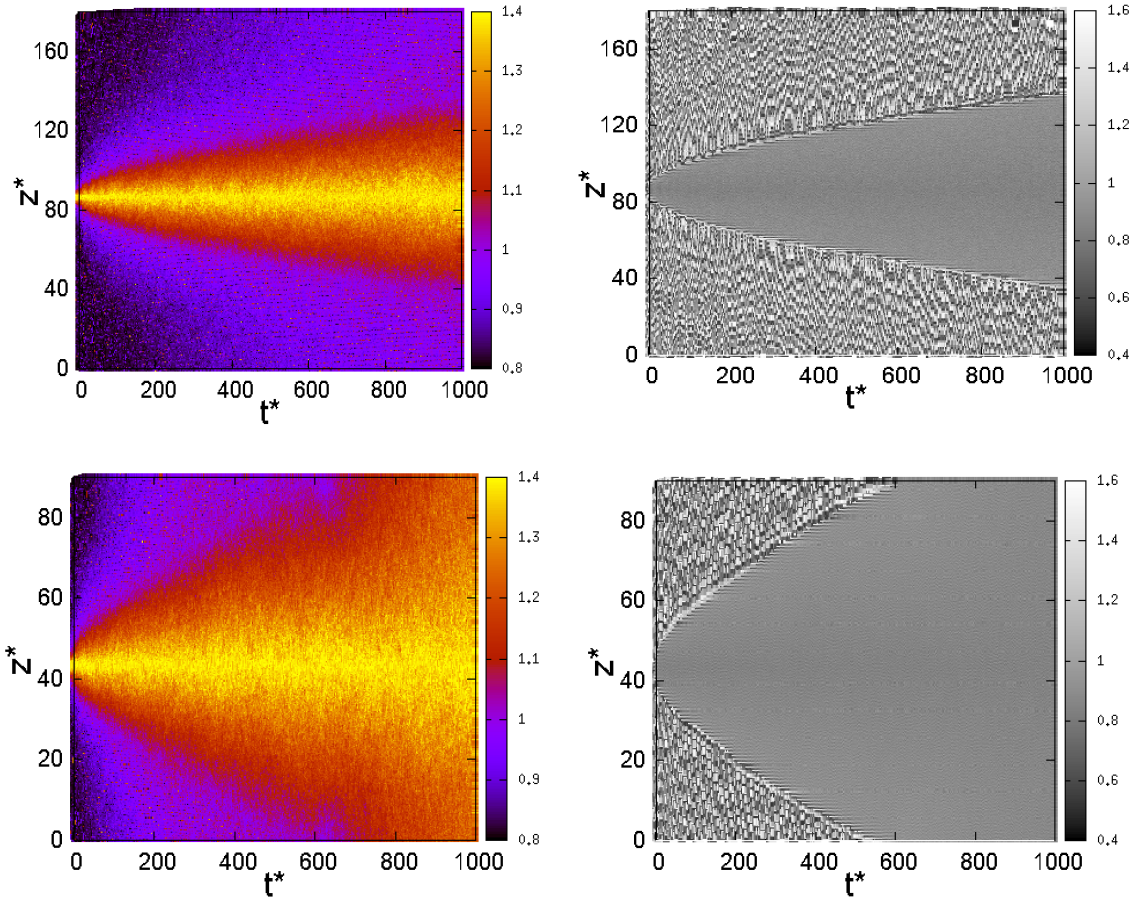


Figure 4: Evolution of the temperature (left) and density (right) with time (t*) for transient processes simulated with different system sizes, (top panels) 112 (87808 atoms) and (bottom panels) 56 (43904 atoms) unit cells in the z direction of the simulation cell. The color / grey scales represent different temperatures (left panels) / densities (right panels) observed during the transient process. All the simulation correspond to the systems at $P^* = 3.893$ with the temperature of the thermostat set to $T^* = 1.4$.

the characteristic proportionality of the position of the melting front with $\sqrt{t}$. At long times however, the Neumann solution becomes inaccurate. We can assert that this deviation is

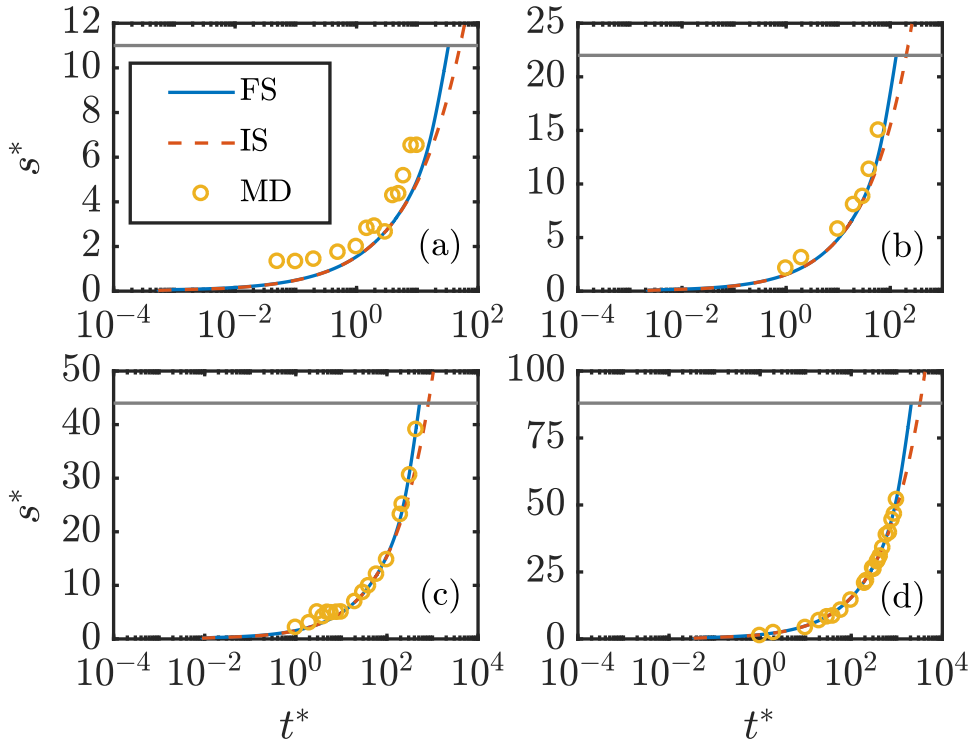


Figure 5: Time dependence of the position of the melting front for systems of different size, (14,14,N_z), with N_z = 14, 28, 56, 112. The symbols were obtained from the analysis of the MD simulations. The lines represent the theoretical results for the infinite system, Eq. (11), and the numerical solution corresponding to the finite system (section B-b). The horizontal lines correspond to $s^* = L_z^*/2$ with L_z^* = 22.22, 44.45, 88.89, 177.78 (for N_z = 14, 28, 56, 112, respectively) and indicate completion of melting. The simulation conditions for temperature and pressure are the same as in Figure 4.

connected to the finite size of the simulation box. This idea is confirmed by the numerical solution of the FS model, which takes into account finite size effects, and that shows excellent agreement up to the end of the melting process. The good agreement between the simulation and the continuum models (IS and FS) deteriorates for the shorter simulation boxes (see *e.g.* 14 and 28 lattices in panels 5-(a) and (b), respectively).

As noted above, deviations between the simulation results and the continuum predictions are expected at time $t \leq \tau_{J_q}$. This point was noted in previous studies.[16] The reason for the discrepancy was not specified but it was suggested that it could not be attributed to mechanical effects (e.g., thermal expansion) which, as in the present work, were not included

into the continuum model, or to the temperature dependence of the thermal conductivity. However, in our case the deviation extend several times τ_{J_q}. We argue that the reason for the deviation is specific to the transient melting process studied here, particularly to the fact that melting does not take place immediately upon switching on the thermostat. Homogeneous melting is an activated process and consequently it involves a characteristic time scale that depends on the difference between the temperature of the thermostat and the melting temperature, as well as on the activation energy of formation of the critical nucleus of the liquid phase. We show in Figure 6 a sequence of configurations at different times in the interval $t^* \in [0, 6]$ (≈0-13 ps) that illustrate the melting process induced by local heating. We have identified particles belonging to solid (FCC) or liquid phases by using the common neighbor analysis method[35] with the adaptive approach introduced in reference.[36] These methods identify the local atomic structure using a distance criterion in combination with an analysis of the number of nearest neighbors. Upon switching on the thermostat in the middle of the cell the FCC structure is disrupted (see times $t^* = 0.2$ and $t^* = 1.0$). However, the FCC order is still present at the center of the thermostat at $t^* = 2.0$ (4.3 ps), and the order eventually disappears at longer times. The activation of the melting process takes place in characteristic times scales of the order of 5 ps, which is the timescale where the internal energy converges towards the $\sqrt{t}$ dependence predicted by the continuum model (see left panel in Figure 7). The simulations therefore show a breakdown of the continuum solution at timescales < 5 ps, which we interpret as a limitation of the continuum approach to take into account the activated nature of melting, and the co-existence of an additional timescale associated to the formation of the melting front.

The transient melting process is accompanied by a concomitant increase of the internal energy. Theoretically, the time dependence of the energy is defined by the temperature of the solid and liquid phases as well as by the position of the melting front (equations (13)-(17)). The linear dependence with the position of the front, $s(t)$, defines the time dependence of the energy too, $\sqrt{t}$. This dependence is reproduced by the simulations at long times, typically

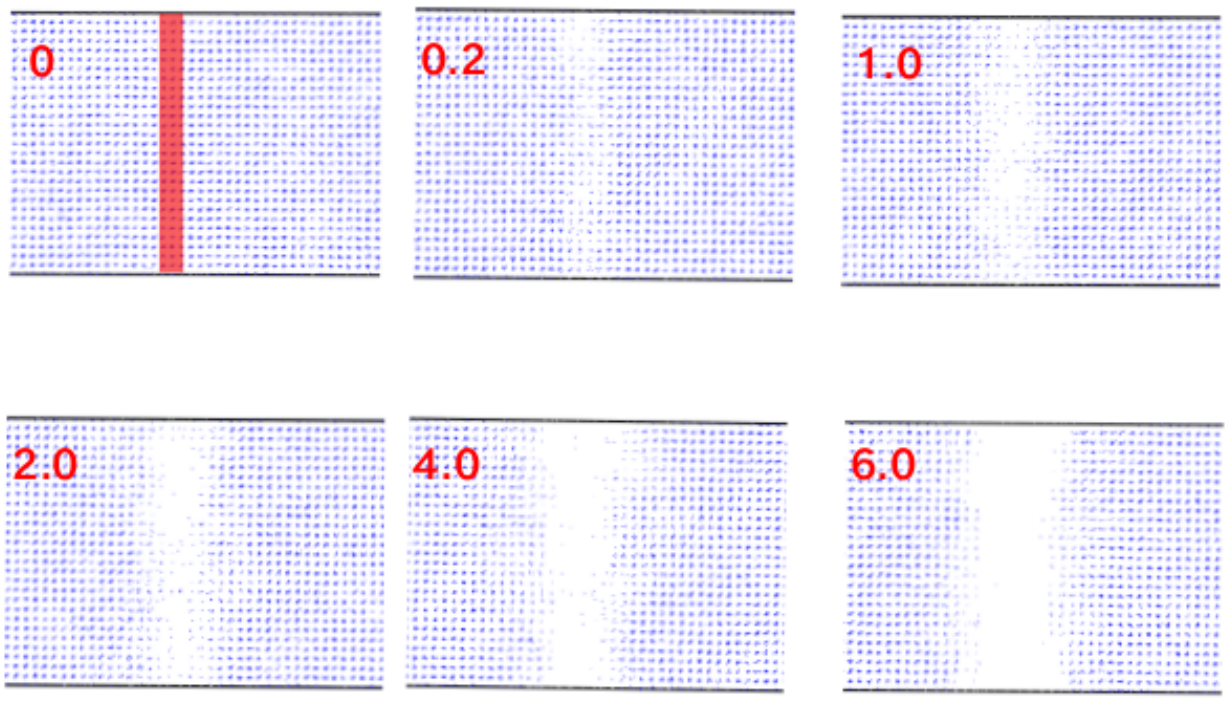


Figure 6: Sequence of snapshots showing the transient melting process at early stages from $t^* = 0$ to $t^* = 6$. The blue dots represent the position of atoms with the FCC structure according to the common neighbor analysis.[35,36] The red vertical band represents the position of the thermostat. The snapshots correspond to the system with $N_z = 112$ and melting temperature $T_m^* = 1.0$, $P^* = 3.893$ and temperature of the thermostat $T^* = 1.4$.

$t^* > 2$ (~ 5 ps) as shown in Figure 7 (left panel). While we find significant deviations at short times, deviations are observed at longer times too, with the simulated data departing from the $\sqrt{t}$ dependence. These deviations are connected to the completion of the melting process and, later, to the heating of a homogeneous fluid until the whole system reaches the temperature of the thermostat. The characteristic time for the temperature profile to fulfill $T(z) > T_m \ \forall z$ varies with the system size: $t^* = 14$ (30 ps), 60.2 (130 ps) and 300 (650 ps) for $N_z = 14$, 28 and 56, respectively.

We compare in Figure 7 the simulated internal energies and the predictions from the continuum theory using the IS and FS models described in Section 3. To calculate the internal energy using the continuum approach we employed the heat capacities, densities, thermal

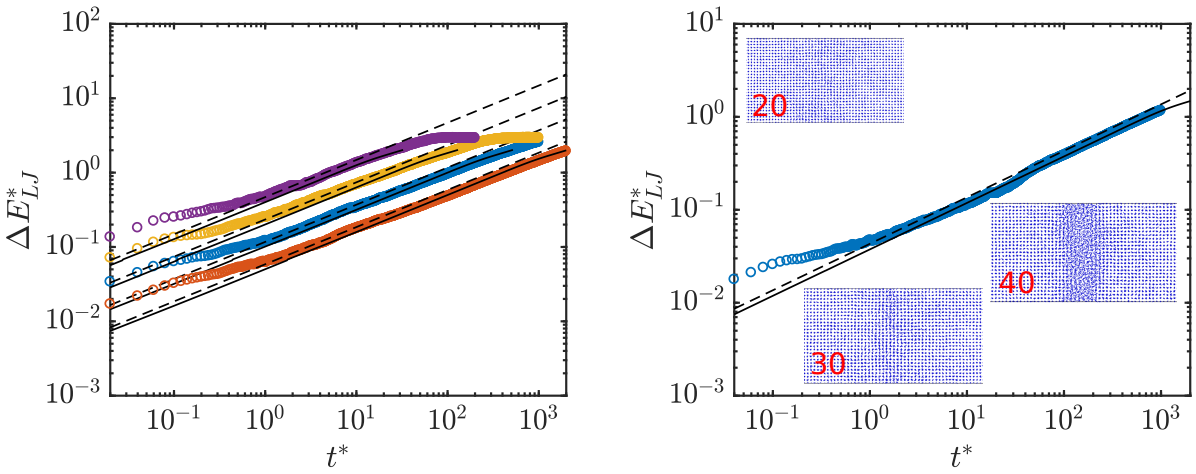


Figure 7: (Left) Internal energy as a function of time for simulation boxes of different sizes (14,14,N_z) with (from top to bottom) $N_z = 14, 28, 56, 112$. The dashed lines represent the $\sqrt{t}$ dependence predicted by the IS model and the solid lines the energy predicted by the FS model. The internal energy is represented as the energy per particle in Lennard-Jones units. (Right) Same as left panel for $N_z = 112$ and thermostat temperature $T^* = 1.25$. The snapshots represent the configuration at different times, $t^* = 20$, 30 and 40.

conductivities, melting temperature and enthalpy of fusion obtained from the simulations (see Table 1). To obtain a consistent comparison with the simulation, the total energy (17) was divided by the corresponding number of particles for each system and the characteristic energy scale is represented in reduced units, *i.e.* $\Delta E^*_{LJ} = \Delta E/N\varepsilon$ (where $N = 10976$, 21952, 43904, or 87808). The simulation results for thermostat temperature $T^* = 1.4$ (Fig. 7, left panel) deviate significantly from the continuum solution at very short times ($t^* \ll 1$). These times correspond to the early stages of application of the thermostat and barostat and are of the order of the heat flux relaxation times (See Table 1). Therefore, deviations from the continuum solution are expected at these times, and these data were not considered for comparison with the continuum solution. Furthermore, the analytical solution of the IS model (Section 3-a) deviates significantly at long times. Following our observations for the time dependence of the position of the melting front, the deviation at long times is connected to the finite size of the simulation box, which has an impact on the energy contributions derived in equations (13)-(14). To take the finite size effects into account we solved numerically the

FS model (Section 3-b). The results from this model present a $\sqrt{t}$ dependence for most part of the melting process. Near the end of melting the increase of energy slows down, deviating from the $\sqrt{t}$ behaviour and following closely the simulation results, supporting the idea that finite size effects can be well accounted for by the FS model.

We now discuss the temperature profiles obtained using the continuum FS model and the MD simulations, at several times for the systems with $N_z = 56$ and $N_z = 112$. As observed in Fig. 8, the solution of the FS model features a characteristic discontinuity in the thermal gradient, ∇T, at the melting temperature, T_m, which is connected to the Stefan condition (8), which applies to the liquid-solid interface. The simulation results at long times, *i.e.* longer than τ_{J_q} and the pre-melting time ($t^* > 2$, $\sim 5\,\mathrm{ps}$), follow closely the solution of the continuum equation (see, Fig. 8(a)-(b)), and feature a clear discontinuity as well at the correct melting temperature. The agreement with the continuum model is excellent, showing that this model describes accurately the transient melting process at fairly short timescales, $t^* = 20$ ($\approx 40\,\mathrm{ps}$). We note that the continuum solution assumes a constant thermal conductivity for the liquid and solid phases. The thermal conductivity will change when the temperature and densities are different from the coexistence ones, but the good agreement between theory and simulation indicates that such effects are minor for simple atomic solids and do not introduce significant deviations between the simulation results and the continuum solution.

We have represented in panels (c) and (d) from Figure 8 the theoretical predictions and simulation results for short times, $t^* = 2$ ($\approx 4\,\mathrm{ps}$), where we found deviations between the continuum theory and simulations (see Figure 7 and the associated discussion). At these times, deviations become apparent in the temperature profiles as well, highlighting the limitations of the continuum approach in the description of the very early stages of the transient melting. It is worth mentioning that mechanical waves (due to thermal expansion) or thermal waves (second sound effect) are not expected to be dominant at times larger than $t^* \approx 2$ in our simulations. We can compute an approximate time scale for the thermal and

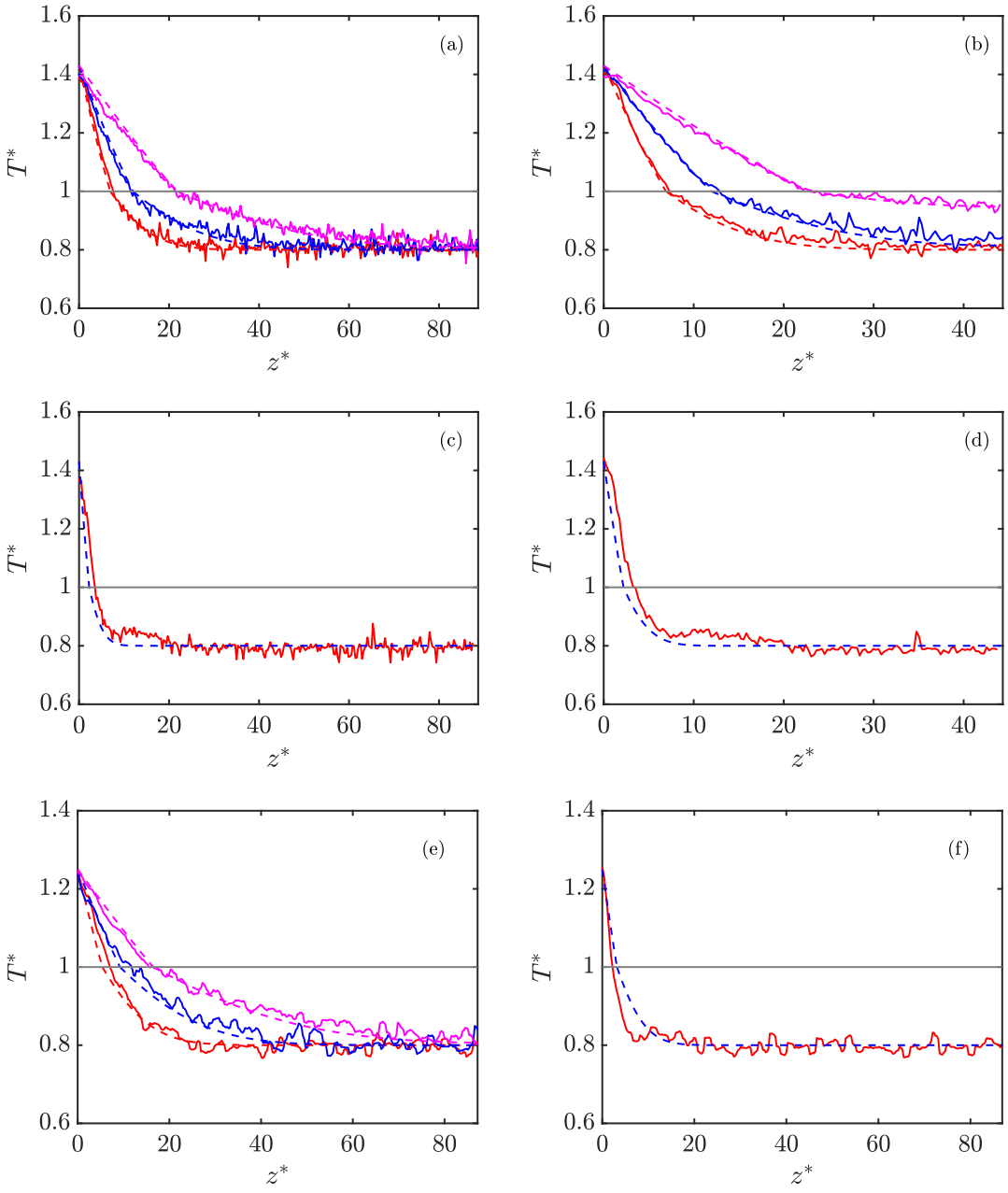


Figure 8: Panels (a)-(b): Temperature profiles at $t^* = 20$, $t^* = 60$, and $t^* = 200$, for the systems $N_z = 112$ (left) and $N_z = 56$ (right). Panels (c)-(d): Temperature profiles at small times ($t^* = 2$) for the system $N_z = 112$ (left) and $N_z = 56$ (right). The solid lines represent the MD simulations and the dashed lines the predictions of the FS continuum model. The horizontal line indicates the melting temperature. Panels (e)-(f): Profiles for the system $N_z = 112$ with thermostat temperature $T^* = 1.25$ at times $t^* = 20$, $t^* = 60$, and $t^* = 200$ (left) and at $t^* = 2$ (right).

mechanical waves as follows. Assuming a speed of sound of ~ 3000 m/s,[16] and the largest box considered in our computations, $N_z = 112$, the characteristic time for the sound wave to traverse the box from the center to the edges is $\sim$1 ps ($t^* \sim 0.5$), which is smaller than the time where deviations between MD and continuum theory are found.

Referring to system size effects, we note that it is well known that the Fourier's law breaks down when the size of the physical system is of the same order of magnitude as the mean-free path of the heat carriers.[6,32–34] The relative size of the mean-free path of the heat carriers with respect the size of the system is measured by the Knudsen number $Kn = l/L$ where l is the phonon mean-free path and L the size of the system. In fact, even for $Kn < 1$ and $t > \tau_{J_q}$ discrepancies may still persist when compared to the solution of the Boltzmann equation.[32] The phonon mean-free path can be estimated from the kinetic expression $l = 3\lambda_s/\rho_s c_s v$, where v is the speed of sound. We note that for solid Argon, the kinetic theory predicts phonon mean free paths and relaxation times ($\tau_p = v/l$) that are in agreement with MD simulations and experiments.[37] However, it tends to underestimate l for more complex solids like Silicon, where calculations from kinetic theory at room temperature predict $l = 100\,\text{nm}$ albeit phonons with $l \leq 100\,\text{nm}$ only contribute 20% to total energy conduction.[38] In our case, by taking $v \approx 3000$ m/s from[16] (similar densities and temperatures) and using the parameter values for the solid phase from Table 1 scaled to dimensional units, *i.e.* the density $\rho_s = 1691\ \text{kg m}^{-3}$, heat capacity $c_s = 863\ \text{J K}^{-1}\ \text{kg}^{-1}$ and thermal conductivity $\lambda_s = 0.23\ \text{W m}^{-1}\,\text{K}^{-1}$, we get $l \sim 0.2\,\text{nm}$. Previous studies reported $l = 0.71 - 6.15\,\text{nm}$ in the temperature range $20 - 70\,\text{K}$ for argon crystals,[39] where the lowest value for l corresponds to the highest temperature (70 K). Using $l \approx 0.2\,\text{nm}$, gives Knudsen numbers $Kn = 0.0132$, $Kn = 0.0066$, $Kn = 0.0033$, $Kn = 0.0017$ for our four system sizes. So, the size of our system is large as compared to the mean free path, hence supporting our hypothesis that the deviations at $t > \tau_{J_q}$ are related to the emergence of other timescales connected to the melting process.

In order to further investigate the activated nature of the melting process, we have

performed more simulations for the system $N_z = 112$ and setting the temperature of the thermostat at $T^* = 1.25$. If the process is activated we expect that the lower temperature of the thermostat relative to the melting temperature should result in an increase of the time required to recover the continuum solution, since the melting of the solid will take longer times. We show in Fig. 7 (right panel) the evolution of the internal energy as a function of time. We find that the deviations between continuum theory and the simulation are indeed observed at longer times $t^* \lessapprox 35$. We have included in Fig. 7 representative snapshots of the configuration at different times. The snapshots show indeed that the solid has not melted at time $t^* = 30$ and remains in a superheated metastable state, while melting in the center of the cell has taken place at time $t^* = 40$. The melting event is reflected in a sigmoid change in the internal energy with a faster increase of the energy (see times $t^* \sim 35$).

Finally, in panels (e)-(f) from Figure 8 we show the temperature profiles for the $T^* = 1.25$ case at the same times as the case $T^* = 1.4$. For $T^* = 1.25$ and $t^* = 20$ the deviations between the simulated and continuum solution appear larger than for the case $T^* = 1.4$ at the same time (see Fig. 8, panel (a)); there is not an obvious change in slope around the melting temperature, while this is observed in the $T^* = 1.4$ case. However, we note that a direct comparison of the temperature profiles may lead to the wrong conclusion that the continuum and simulated result may appear in good agreement, even at short times. We therefore favor the use of the internal energy (Figure 7) as a more stringent test of the validity of the continuum solution. At very short times, $t^* = 2$ (panel (f)) the discrepancies between the heat diffusion solution and the simulation are evident, in agreement with our results for the $T^* = 1.4$ case.

5 Conclusions and Final Remarks

We have performed a numerical investigation of the melting process of simple atomic solids using both theoretical solutions of the heat diffusion equation and transient non-equilibrium

molecular dynamics simulations. We find that the continuum solution predicts accurately the transient process at long times, specifically: the speed of the melting front, evolution of the internal energy with the correct time dependence $\sqrt{t}$ and the transient temperature profile. The latter is of particular interest since such profile can be used to identify the correct melting temperature of a solid with little computational effort. This does not represent a huge challenge for atomistic systems investigated here, but could offer definite advantages in the analysis of more complex molecular solids. The implementation of the method in more complex settings will require an analysis of the finite size dependence of the results.

We have shown that very small systems, normally used in computer simulations, can not be described accurately using the standard HDE, while the finite size effects can be accounted for with the continuum approach when the HDE is coupled to boundary conditions appropriate to describe melting processes in finite domains.

We have identified a breakdown of the continuum solution at short times. Although this is expected as noted by previous authors when the relevant time is shorter than the correlation time for the relaxation of the heat flux, we have identified additional sources of the deviation, which are evident at times $\lessapprox 5$ ps or $\lessapprox 80$ ps for thermostat temperatures 40% and 25%, respectively, above the melting temperature. We associate the emergence of these additional timescales to the activation energies required to melt the solid phase. Hence, we expect that the the application of the heat diffusion equation to interpret transient melting will depend on the degree of superheating of the systems with respect to the thermodynamic melting temperature, and the time needed to recover the continuum solution will increase as the degree of superheating decreases. This effect should be taken into account in the interpretation of short time transient melting processes.

Acknowledgement

We thank the EPSRC-UK (EP/J003859/1) for financial support. FF research was partially

supported by the Royal Irish Academy through a Charlemont Grant 2016. We acknowledge the Imperial College High Performance Computing Service for providing computational resources. We acknowledge two anonymous referees for insightful comments.

References

(1) Incropera, F.; DeWitt, D.; Bergman, T.; Lavine, A. *Fundamentals of Heat and Mass Transfer*; John Wiley & Sons: Hoboken, 2006.

(2) Cahill, D.; Braun, P.; Chen, G.; Clarke, D.; Fan, S.; Goodson, K.; Keblisnki, P.; King, W.; Mahan, G.; Majumdar, A.; Marris, H.; Philpott, S.; Pop, E.; Shi, L. Nanoscale thermal transport. II. 2003-2012. *Appl. Phys. Rev.* **2014**, *1*, 011305.

(3) Tascini, A. S.; Armstrong, J.; Chiavazzo, E.; Fasano, M.; Asinari, P.; Bresme, F. Thermal transport across nanoparticle-fluid interfaces: the interplay of interfacial curvature and nanoparticle-fluid interactions. *Phys. Chem. Chem. Phys.* **2017**, *19*, 3244–3253.

(4) Ge, Z.; Cahill, D. G.; Braun, P. V. AuPd metal nanoparticles as probes of nanoscale thermal transport in aqueous solution. *J. Phys. Chem. B* **2004**, *108*, 18870–18875.

(5) Wagner, G.; Jones, R.; Templeton, J.; Parks, M. An atomistic-to-continuum coupling method for heat transfer in solids. *Comput. Methods Appl. Mech. Eng.* **2008**, *197*, 3351–3365.

(6) Alvarez, F. X.; Jou, D. Memory and nonlocal effects in heat transport: From diffusive to ballistic regimes. *Appl. Phys. Lett.* **2007**, *90*, 2005–2008.

(7) Clark, J. N.; Beitra, L.; Xiong, G.; Fritz, D. M.; Lemke, H. T.; Zhu, D.; Chollet, M.; Williams, G. J.; Messerschmidt, M. M.; Abbey, B.; Harder, R. J.; Korsunsky, A. M.; Wark, J. S.; Reis, D. A.; Robinson, I. K. Imaging transient melting of a nanocrystal using an X-ray laser. *Proc. Natl. Acad. Sci.* **2015**, *112*, 7444–7448.

(8) Merabia, S.; Shenogin, S.; Joly, L.; Keblinski, P.; Barrat, J.-L. Heat transfer from nanoparticles: a corresponding state analysis. *Proc. Natl. Acad. Sci.* **2009**, *106*, 15113–8.

(9) Stocker, K. M.; Neidhart, S. M.; Gezelter, J. D. Interfacial thermal conductance of thiolate-protected gold nanospheres. *J. Appl. Phys.* **2016**, *119*, 025106.

(10) Font, F.; Myers, T. G. Spherically symmetric nanoparticle melting with a variable phase change temperature. *J. Nanopart. Res.* **2013**, *15*, 2086.

(11) Font, F.; Myers, T. G.; Mitchell, S. L. A mathematical model for nanoparticle melting with density change. *Microfluid. Nanofluidics* **2015**, *18*, 233–243.

(12) Back, J. M.; McCue, S. W.; Moroney, T. J. Including nonequilibrium interface kinetics in a continuum model for melting nanoscaled particles. *Sci. Rep.* **2014**, *4*, 7066.

(13) Chantrenne, P.; Barrat, J.-L. Finite size effects in determination of thermal conductivities: comparing molecular dynamics results with simple models. *J. Heat Transfer* **2004**, *126*, 577–585.

(14) Melis, C.; Dettori, R.; Vandermeulen, S.; Colombo, L. Calculating thermal conductivity in a transient conduction regime: theory and implementation. *Euro. Phys. J. B* **2014**, *87*, 96.

(15) Muscatello, J.; Chacón, E.; Tarazona, P.; Bresme, F. Deconstructing Temperature Gradients across Fluid Interfaces: The Structural Origin of the Thermal Resistance of Liquid-Vapor Interfaces. *Phys. Rev. Lett.* **2017**, *119*, 045901.

(16) Volz, S.; Saulnier, J.-B.; Lallemand, M.; Perrin, B.; Depondt, P.; Mareschal, M. Transient Fourier-law deviation by molecular dynamics in solid argon. *Phy. Rev. B* **1996**, *54*, 340–347.

(17) Mastny, E. A.; de Pablo, J. J. Melting line of the Lennard-Jones system, infinite size, and full potential. *J. Chem. Phys.* **2007**, *127*.

(18) Heinz, H.; Vaia, R. A.; Farmer, B. L.; Naik, R. R. Accurate Simulation of Surfaces and Interfaces of Face-Centered Cubic Metals Using 12-6 and 9-6 Lennard-Jones Potentials. *J. Phys. Chem. C* **2008**, *112*, 17281–17290.

(19) G.C. Maitland, M. Rigby, E.B. Smith and W.A. Wakeham, *Intermolecular forces: their origin and determination*; Clarendon Press: Oxford, 1971.

(20) Plimpton, S. Fast Parallel Algorithms for Short-Range Molecular Dynamics. *J. Comp. Phys.* **1995**, *117*, 1–19.

(21) Berendsen, H. J. C.; Postma, J. P. M.; van Gunsteren, W. F.; DiNola, A.; Haak, J. R. Molecular dynamics with coupling to an external bath. *J. Chem. Phys.* **1984**, *81*, 3684–3690.

(22) Laird, B. B.; Davidchack, R. L. Direct calculation of the crystal-melt interfacial free energy via molecular dynamics computer simulation. *J. Phys. Chem. B* **2005**, *109*, 17802–17812.

(23) Zwanzig, R. Time-Correlation Functions and Transport Coefficients in Statistical Mechanics. *Annu. Rev. Phys.* **1965**, *16*, 67–102.

(24) Irving, J. H.; Kirkwood, J. G. The Statistical Mechanical Theory of Transport Processes. IV. The Equations of Hydrodynamics. *J. Chem. Phys.* **1950**, *18*, 817.

(25) Alexiades, V.; Solomon, A. *Mathematical modelling of freezing and melting processes*, 1st ed.; Hemisphere Publishing Corporation, 1993.

(26) Liang, Z.; Evans, W. J.; Keblinski, P. Thermal resistance at an interface between a crystal and its melt. *J. Chem. Phys.* **2014**, *141*, 014706.

(27) Gupta, S. *The Classical Stefan Problem: Basic Concepts, Modelling and Analysis with Quasi-Analytical Solutions and Methods*, 2nd ed.; Elsevier, 2017.

(28) Crank, J. *Free and Moving Boundary Problems*, 1st ed.; Oxford University Press, 1996.

(29) Caldwell, J.; Kwan, Y. Y. Numerical methods for one-dimensional Stefan problems. *Comm. Numer. Meth. Eng.* **2004**, *20*, 535–545.

(30) Mitchell, S. L.; Vynnycky, M. Finite-difference methods with increased accuracy and correct initialization for onedimensional Stefan problems. *Appl. Math. Comput.* **2009**, *215*, 1609–1621.

(31) MATLAB and Statistics Toolbox Release 2012b, The MathWorks, Inc., Natick, Massachusetts, United States., **2012**,

(32) Chen, G. Ballistic-Diffusive Equations for Transient Heat Conduction From Nano to Macroscales. *J. Heat Transfer* **2001**, *124*, 320–328.

(33) Chen, G. Particularities of Heat Conduction in Nanostructures. *J. Nanopart. Res.* **2000**, *2*, 199–204.

(34) Chen, G. Ballistic-Diffusive Heat-Conduction Equations. *Phys. Rev. Lett.* **2001**, *86*, 2297–2300.

(35) Honeycutt, J. D.; Andersen, H. C. Molecular dynamics study of melting and freezing of small Lennard-Jones clusters. *J. Phys. Chem.* **1987**, *91*, 4950–4963.

(36) Stukowski, A. Structure identification methods for atomistic simulations of crystalline materials. *Model. Simul. Mater. Sci. Eng.* **2012**, *20*, 045021.

(37) Tretiakov, K. V.; Scandolo, S. Thermal conductivity of solid argon from molecular dynamics simulations. *J. Chem. Phys.* **2004**, *120*, 3765–3769.

(38) Henry, A. S.; Chen, G. Spectral Phonon Transport Properties of Silicon Based on Molecular Dynamics Simulations and Lattice Dynamics. *J. Comput. Theor. Nanosci.* **2008**, *5*, 141–152.

(39) Ju, S.; Liang, X. Investigation of argon nanocrystalline thermal conductivity by molecular dynamics simulation. *J. Appl. Phys.* **2010**, *108*, 104307.

Graphical TOC Entry

